Field-induced reentrant magnetoelectric phase in $LiNiPO_4$

Rasmus Toft-Petersen,[1,*] Ellen Fogh,[2] Takumi Kihara,[3] Jens Jensen,[4] Katharina Fritsch,[1] Jooseop Lee,[5] Garrett E. Granroth,[6] Matthew B. Stone,[5] David Vaknin,[7] Hiroyuki Nojiri,[3] and Niels Bech Christensen[2]

[1]*Helmholtz Zentrum Berlin für Materialien und Energie, D-14109 Berlin, Germany*

[2]*Department of Physics, Technical University of Denmark, DK-2880 Kongens Lyngby, Denmark*

[3]*Institute for Materials Research, Tohoku University, Sendai 980-8577, Japan*

[4]*Niels Bohr Institute, Universitetsparken 5, DK-2100 Copenhagen, Denmark*

[5]*Quantum Condensed Matter Division, Oak Ridge National Laboratory, Oak Ridge, Tennessee 37831, USA*

[6]*Neutron Data Analysis and Visualization Division, Oak Ridge National Laboratory, Oak Ridge, Tennessee 37831, USA*

[7]*Ames Laboratory and Department of Physics and Astronomy, Iowa State University, Ames, Iowa 50011, USA*

(Received 1 April 2016; revised manuscript received 20 January 2017; published 21 February 2017)

Using pulsed magnetic fields up to 30 T we have measured the bulk magnetization and electrical polarization of $LiNiPO_4$ and have studied its magnetic structure by time-of-flight neutron Laue diffraction. Our data establish the existence of a reentrant magnetoelectric phase between 19 T and 21 T. We show that a magnetized version of the zero field commensurate structure explains the magnetoelectric response quantitatively. The stability of this structure suggests a field-dependent spin anisotropy. Above 21 T, a magnetoelectrically inactive, short-wavelength incommensurate structure is identified. Our results demonstrate the combination of pulsed fields with epithermal neutron Laue diffraction as a powerful method to probe even complex phase diagrams in strong magnetic fields.

DOI: 10.1103/PhysRevB.95.064421

I. INTRODUCTION

The coupling between magnetization and ferroelectricity in magnetoelectric (ME) materials [1–3] suggests a wide range of prospects for applications [4]. Low-power ME memory devices are currently being realized [5–9] and electrically manipulating spin waves to process information has far-reaching perspectives [10–12]. These low-symmetry materials offer a menagerie of possible microscopic origins for the ME coupling, including incommensurate (IC) magnetic structures in frustrated magnets [13] and transition metal orbital magnetism [14]. For instance, $TbMnO_3$ has a complex magnetic phase diagram with two distinct multiferroic phases [15,16], where a cycloid IC structure produces ferroelectric polarization [17]. Another example is $MnWO_4$, where electric polarization is generated by an elliptical spiral [18], the chirality of which can be controlled by an electric field [19]. In Cr_2O_3, multiple coexisting mechanisms may even be possible [20,21].

The $S = 1$ Ni^{2+} ions in orthorhombic $LiNiPO_4$ (space group $Pnma$ with lattice parameters $a = 10.02$ Å, $b = 5.83$ Å, and $c = 4.66$ Å) [22–25] form a frustrated 3D antiferromagnetic network. Its spin dynamics is dominated by the competition between nearest (J_1) and next-nearest (J_2) neighbor interactions in the bc plane [26,27]. The c axis is the easy axis, but the anisotropy within the ac plane is weak. The combination of spin anisotropy and a prominent Dzyaloshinskii-Moriya (DM) interaction results in commensurate magnetic order below $T_N = 20.7$ K and—for magnetic fields along the easy c-axis—in a ME response P_x caused by field-induced canting of the spins [28]. The ratio of J_1 to J_2 leaves $LiNiPO_4$ near an instability to IC magnetic order. Indeed, the low-temperature commensurate phase is bordered by IC phases (with collinear and spiral spin structures, respectively) above T_N in zero field [29] and above 12 T parallel to c at 1.5 K [28,30]. Both of these phases are magnetoelectrically inactive. At 16 T the IC modulation of the spiral locks into a quintupling of the crystallographic unit cell along b. Pulsed field magnetization measurements at 4.2 K indicate the existence of additional magnetic phase transitions for fields in the range 14–22 T [31]. The ME properties and magnetic structures of the higher-field phases are unknown, but recent advances in pulsed-field diffraction [32–35] imply that the latter can now be investigated using neutron scattering.

We use pulsed magnetic fields to study the magnetization, electrical polarization, and magnetic structures of $LiNiPO_4$ up to 30 T along the c axis. Our results demonstrate how epithermal neutron Laue diffraction in pulsed fields allows an efficient and exhaustive identification of propagation vectors characterizing a complex sequence of magnetic phases. We show that magnetoelectricity reemerges in the field range 19–21 T and is accompanied by commensurate antiferromagnetic order with spins polarized along the applied field axis. This phase is supplanted by a magnetoelectrically inactive, short-wavelength IC structure above 21 T. Combining the bulk and neutron diffraction data, a quantitative model connecting the magnetic structures, magnetization process, and magnetoelectric response of $LiNiPO_4$ is developed. Finally, we discuss whether a drastic field dependence of the spin-anisotropy can explain the observed magnetic structure. Our results establish $LiNiPO_4$ as a model system with a complex phase diagram that is directly impacted by the spin-lattice coupling.

II. EXPERIMENTAL DETAILS

The neutron diffraction experiment was performed on the SEQUOIA direct time-of-flight spectrometer [36] at the Spallation Neutron Source, Oak Ridge National Laboratory. The instrument was operated in Laue mode with an epithermal neutron wavelength band $\lambda = 0.1$–0.8 Å. The pulsed magnetic field was generated by a solenoid coil, mounted in an insert for a standard ^{4}He -flow cryostat, and connected to a capacitor

*Present address: Department of Physics, Technical University of Denmark, DK-2880 Kongens Lyngby, Denmark.

bank delivering 4–5 ms pulses and a maximum field of 30 T. This setup [32,33] allows the sample temperature to be controlled by the cryostat, while the solenoid is immersed in liquid nitrogen. A high-quality single crystal ($m \approx 400$ mg [29]) was mounted inside the 12 mm magnet bore with its crystallographic a axis vertical and the c axis at an angle $\theta = 2.8^\circ$ away from the field axis, which in turn was parallel to the incident beam. With this crystal orientation, momentum transfers parallel to $(0,1,0)$ are probed at a horizontal scattering angle 2θ.

The existence of specific Bragg peaks $\mathbf{Q} = (0,K,0)$ can now be investigated by adjusting the maximum field $\mu_0 H_{\max}$ and the time delay Δt between the magnet pulse and the neutron pulse emanating from the spallation target (see Appendix A and Fig. 4). Neutrons fulfilling the condition $Q = (2\pi/b)K = (4\pi/\lambda)\sin(\theta)$ then arrive at the sample position while the field takes on a value in the range of interest. Employing the time-of-flight method, the neutron wavelength λ, and therefore K, depends on time. With each setting, Bragg peaks are probed along a curve in a $\mu_0 H_z$ versus K plane [see Fig. 2(a)].

The advantage of using epithermal neutrons is that the momentum range probed near the field maximum is comparable to typical Brillouin zone dimensions. Further, the decrease in Bragg peak reflectivity associated with the use of short-wavelength neutrons is partially compensated by a reduction in absorbtion and extinction losses [37]. The cooling requirements of the coil limit the number of pulses to 6–10 per hour, leaving only the strongest Bragg peaks observable.

In addition to the diffraction experiment, the magnetization and electrical polarization were measured in pulsed fields up to 30 T applied along the c axis. The pulse durations (FWHM) were 5 ms and 2 ms, respectively. The absolute value of the magnetization m was scaled to previous results obtained with static fields [30]. The electrical polarization was measured using a procedure similar to that described in Refs. [38,39]. All measurements presented in this paper were obtained at $T = 4.2$ K.

III. RESULTS

The bulk magnetization shown in Fig. 1(a) indicates the existence of five phases at 4.2 K (enumerated I–V with increasing field) up to 30 T where the magnetization approaches $(1/3)m_S$, with the expected saturation magnetization per ion given by $m_S \simeq 2.2\mu_B$. The associated critical fields are in rough agreement with those reported in Ref. [31]. The two lowest transition fields at 12 and 16 T are in agreement with our previous studies [28,30]. The ME response $P_x = \alpha_{xz} H_z$ of the five phases is shown in Fig. 1(b). At low fields in phase I, the known linear ME effect of $LiNiPO_4$ [22,28], is observed. At fields larger than ~ 6.5 T, a quadratic component develops before the polarization drops to zero at the transition from the commensurate phase I to the IC screw spiral phase II. P_x remains zero as the spiral structure reestablishes commensuration with the lattice [30] in phase III. In phase IV a dramatic reentrance of ME effect is observed, with P_x increasing linearly with field before disappearing at the transition to phase V.

We note that there are slight variations between the transition fields seen in the magnetization and polarization measurements. These are likely due to the differences in pulse duration and shape. Furthermore, phase coexistence and demagnetization effects are expected to be more pronounced for pulsed fields as compared to static fields. Additionally, both data sets display hysteresis as is typical for first-order transitions.

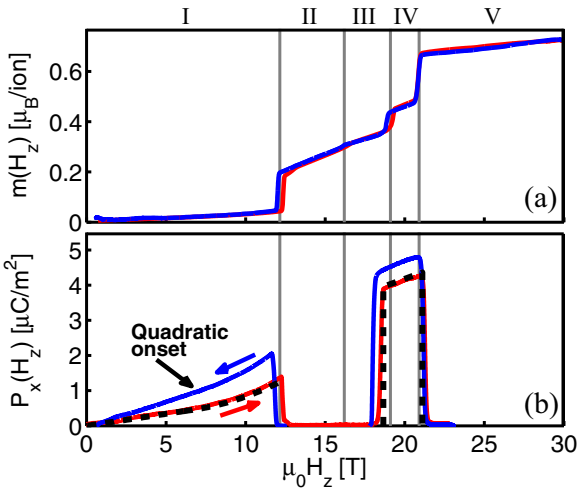

FIG. 1. Magnetization m (a) and electrical polarization P_x (b) at 4.2 K versus $\mu_0 H_z$. The solid vertical lines at $\mu_0 H_z \simeq 12$ T, 16 T, 19 T, and 21 T are approximate transition fields deduced from the magnetization and its derivative. The polarization data indicate a finite ME response in phases I ($\mu_0 H_z \leqslant 12$ T) and IV (19 T $\leqslant \mu_0 H_z \leqslant$ 21 T). The dashed line corresponds to the model calculation described in the text.

Next, we describe the pulsed field neutron diffraction results. Figure 2(a) shows all data obtained for $\mu_0 H_z > 10$ T. Each circle represents a single neutron recorded by a small number of detector pixels near the horizontal scattering angle 2θ (see Appendix A for details). The curved, solid lines represent corresponding values of $(0,K,0)$ and $\mu_0 H_z$ for each field pulse setting. A clustering of neutrons near specific values of K is evident in each of the magnetic phases. Note in particular that the nuclear $(0,2,0)$ reflection is observed for all magnet pulses, in the field interval 0–21 T, demonstrating that the sample maintains its orientation throughout the experiment. In Figs. 2(b)–2(d) we integrate the detected neutron counts over the field ranges of phases III, IV, and V. The peak positions are then extracted by fitting the resulting curves to Gaussian line shapes. The peak widths were fixed to values obtained by extrapolation from high-statistics measurements of the $(0,1,0)$ and $(0,2,0)$ Bragg peaks performed in zero field (see Appendix A).

From the data in Fig. 2(b), we verify the known propagation vector $(0,0.8,0)$ of phase III. Figure 2(c) shows a main result of our work: the novel magnetoelectric phase IV is characterized by a single propagation vector $(0,0.99(1),0)$ which is equal to $(0,1,0)$ within error. Therefore, the two magnetoelectric phases I and IV of $LiNiPO_4$ are characterized by identical propagation vectors. Finally, Fig. 2(d) indicates the presence of two Bragg reflections, $(0,0.99(1),0)$ and $(0,1.33(1),0)$, in phase V. Due to the possibility of phase coexistence near phase boundaries, the existence of the former peak should be treated with caution and is subject to further investigation.

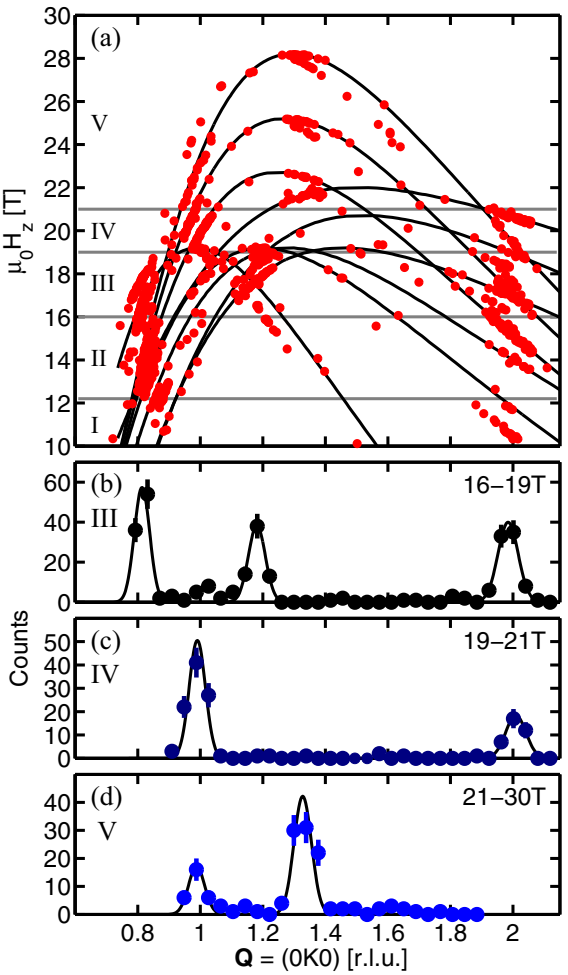

FIG. 2. (a) Raw neutron Laue diffraction data. Each marker represents a single detected neutron. The neutrons probe Bragg peaks on the $(\mu_0 H_z, K)$ curves (solid lines) depending on the maximum field and pulse timing. The horizontal lines represent the transition fields obtained from the magnetization data. Panels (b)–(d) show integrated neutron counts in the field intervals of phases III, IV, and V, normalized to 100 neutron pulses. The Q range is limited to wave vector transfers covered by one or more pulses in the respective magnetic phases.

IV. DISCUSSION

A. Magnetic structure in phase IV

The measured magnetization and propagation vector allow us to establish a quantitative model for the electric polarization in phase IV. In this section we show how the most probable magnetic structure consistent with the measured magnetization and electric polarization in Fig. 1 can be identified.

We start by providing an argument showing that the propagation vector in phase IV is commensurate and not incommensurate. The hard axis in $LiNiPO_4$ is along b due to a single-ion anisotropy energy $D_y S_y^2$ with a large $D_y = 1.423$ meV (see Ref. [30] and Appendix C). This serves to confine the magnetic moments to the ac plane. Hence, any magnetic structure characterized by $(0,K,0) = (0,1 \pm k,0)$ has ordered moments perpendicular to the propagation vector. This is the case for the screw spiral structures observed in phases II and III, as well as the sinusoidally modulated structure observed in zero field just above T_N [29,30]. Neither of these structures support the linear ME effect [40]. On the other hand, the commensurate structure in phase I does support the ME effect. This suggests that because a finite electrical polarization is observed in phase IV, its propagation vector is truly commensurate and equal to $(0,1,0)$. The neutron diffraction data give rise to the same conclusion.

We proceed to determine the most probable structure by help of symmetry analysis [28,30]. The four Ni^{2+} ions reside in a nearly face-centered orthorhombic arrangement at $\mathbf{r}_1 = (0.275,0.25,0.98)$, $\mathbf{r}_2 = (0.775,0.25,0.52)$, $\mathbf{r}_3 = (0.725,0.75,0.02)$, and $\mathbf{r}_4 = (0.225,0.75,0.48)$. The magnetic reflections $(0,1 \pm k,0)$ exclusively reflect magnetic ordering of the four ions according to the pattern $C_\gamma = (+,+,-\beta,-\beta)$, where γ denotes the moment direction and $\beta = e^{i\pi k}$ is a phase factor. Here k can be a rational number, corresponding to commensurate propagation vectors, or an irrational number corresponding to an IC propagation vector. In the case of phase IV we have $k = 0$. Other possible symmetry components are $G_\gamma = (+,-,+\beta,-\beta)$, $A_\gamma = (+,-,-\beta,+\beta)$, and $F_\gamma = (+,+,+\beta,+\beta)$. For the momenta $(0,1 \pm k,0)$ probed in our experiment (see Fig. 2), the neutron scattering selection rules imply vanishing intensity contributions from any spin component parallel to b. Thus, $(0,1 \pm k,0)$ peaks reflect *only* C_x and C_z components of the magnetic structure. As shown in Appendix A, the full $\mathbf{Q}$ range probed in the neutron scattering experiment included $(1,1,0)$ and $(1,2,0)$ reflecting G and A symmetry components, respectively. No intensity was observed at these positions and hence we can exclude any major components of these types. Based on the data shown in Figs. 2(b)–2(d) it is estimated that Bragg peaks of ~ 10 times less intensity than the $(0,1,0)$ peak would be impossible to observe in the pulsed-field experiment. On the other hand, the finite magnetization [see Fig. 1(a)] is represented by an F_z component, coexisting with the C_x or C_z component.

We can now exploit the symmetry constraints on the ME effect to choose between these two possibilities, C_x and C_z, for the main magnetic structure components. These constitute two distinct magnetic point groups with two different magnetoelectric tensor components. Thus, a C_x component would lead to the absence of an α_{xz} ME tensor component [2,22,41], in contrast to the observations. On the other hand, a C_z component allows a nonzero α_{xz} element as indeed observed in phase IV. Therefore, we conclude that the main magnetic structure component in phase IV is C_z, just as is the case for the zero-field structure. In zero field, an additional symmetry component, A_x, was observed, resulting in a canting of spin pairs (1, 2) and (3, 4); see Fig. 3(a). In Ref. [28], a small applied field was shown to introduce an asymmetry in this canting angle—represented by a G_x component—in addition to a component F_z reflecting the field-induced magnetization. For phase IV, we propose the version of this structure shown in Fig. 3(b). Here, the spins on sites 1 and 2 are nearly parallel to the applied magnetic field, while those on sites 3 and 4 are rotated away from the c axis. This corresponds to the presence of two additional antiferromagnetic symmetry components of similar magnitude, $A_x \sim G_x$, in addition to the C_z and F_z components deduced from the neutron diffraction and magnetization data, respectively. The squared structure factors for the Bragg peaks

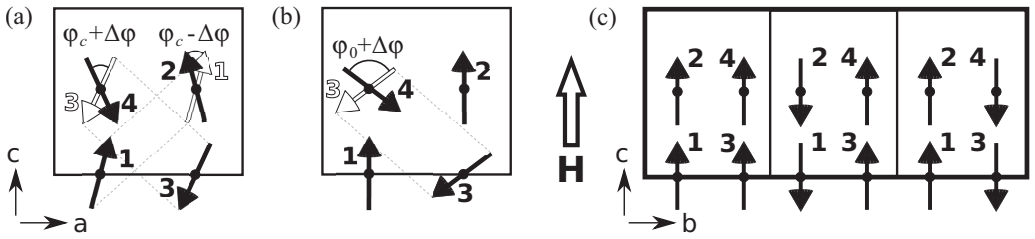

FIG. 3. (a) The magnetic structure in small applied fields in phase I; the difference in spin canting between spin pairs (1, 2) and (3, 4) produces the ME effect [28]. (b) The proposed magnetic structure in phase IV producing the reentrant polarization. The open arrows in (a) and (b) are translated copies of the moments on sublattices 1 and 3, illustrating the relative angles ϕ_c, ϕ_0, and $\Delta\phi(H)$ described in the text. (c) The calculated c components of the IC structure in phase V with $k = 1/3$.

reflecting the A_x and G_x symmetry components correspond to peak intensities about an order of magnitude smaller than the intensity of the observed (0,1,0) peak, and are thus too weak to be observed directly in pulsed fields. However, the existence of these symmetry components is made plausible by the quantitative model for the ME response in both phases I and IV as described in the next section.

Generally, in simple Heisenberg antiferromagnets a spin-flop transition is expected for magnetic fields applied along the easy axis [42,43]. The magnitude of the easy-axis anisotropy determines the spin-flop transition field at which the spins reorient from configurations parallel and antiparallel to the field, to one in which they are transverse to the field. In the transverse configurations spins may gradually turn towards the field direction whereas in a longitudinal structure Zeeman energy can only be gained at $T = 0$ by flipping a spin. With weak ac-plane anisotropy the transverse configuration is therefore favorable in terms of the balance between Zeeman and exchange energy. In addition, the C_x component is experimentally observed to increase in the elliptical (C_z, C_x) spiral structures in phase II and III. Consequently, the observation of a C_z structure in phase IV instead of a C_x structure is surprising. Indeed, the mean-field model that explains the susceptibility, magnetic structure, and dynamics below 17.3 T [30] predicts a C_x-type structure in phase IV. However, as argued above, the only structure consistent with the observed nonzero α_{xz} ME tensor component is C_z. As we shall show below, the C_z structure is further substantiated by providing a canvas for a quantitative model explaining the field dependence of the ME effect in phase IV.

Within the mean-field model [30], the single-ion anisotropy term (providing a preference for spins being oriented along c within the easy ac plane), $D_x S_x^2$ with $D_x = 0.413$ meV, is far too weak to energetically favor a structure with spins along c in phase IV. Nearly a doubling of D_x is required for the system to prefer a longitudinal C_z structure over a C_x-type spin-flop structure in phase IV. Such a dramatic change of anisotropy can hardly be produced by the perturbation of the crystal field levels by the applied magnetic field. Instead, a change of the crystal field itself is probable. This is due to the low symmetry of the crystal field in $LiNiPO_4$ [44], allowing the spin-orbit interaction to introduce a significant orbital contribution to the otherwise quenched ground state, resulting in relatively strong DM interactions and single-ion anisotropy [28]. Even minor changes in the crystal field could have an important impact on the spin anisotropy. Such a field-induced change in spin anisotropy could be produced by a strong magnetostrictive effect, possibly associated with the shift of PO_4 tetrahedra. When the orbital contribution to the ground state is significant, the magnetic field can even alter the crystal field via orbital magnetism coupled directly to the lattice. Such orbitally induced distortions of the crystal field in applied magnetic fields were calculated for the isostructural compound $LiFePO_4$ in Ref. [14].

B. Magnetoelectric effect in phase IV

Our starting point for modeling the magnetoelectric effect in phase IV is inspired by the model previously developed for phase I in Ref. [28] and the similarities between the magnetic structures in phases I and IV. The magnetic structure in phase I, see Fig. 3(a), is predominantly described by C_z with an additional minor symmetry component A_x causing a small canting angle $\phi_c = 15.5^\circ = 0.27$ rad in zero magnetic field. The magnetic structure in phase IV is similar but with a much more pronounced canting angle; see Fig. 3(b). This canting of predominantly the spins on sites 3 and 4 is described by two distinct and similar antiferromagnetic components $A_x \sim G_x \sim \frac{1}{3}C_z$. While these components are too small to be observable in the neutron data directly, their existence can be deduced from the following model encompassing the ME response in both phases I and IV. At the onset field $\mu_0 H \simeq 19$ T the magnetization in phase IV is $m = 0.45\mu_B \simeq (1/5)m_S$ corresponding to an angle between spins 3 and 4 of $\phi_0 \simeq 105^\circ$. In both phases the applied field along c changes the canting angles by $\Delta\phi$, creating an asymmetry in the superexchange (SE) energy of the two spin pairs (1,2) and (3,4). As a result, the SE energy can be lowered by translating the exchange-mediating PO_4 tetrahedra by a distance x along the a axis, leading to an increase (reduction) of the J_{34} (J_{12}) exchange couplings [28]. The corresponding SE energy of the two spin pairs in phase IV is $\mathcal{H}^{\rm SE}_{12,34} = J_{34}\langle S\rangle^2\cos[\phi_0 + \Delta\phi(H)] + J_{12}\langle S\rangle^2 \approx J_{34}\langle S\rangle^2[-0.26 - 0.97\Delta\phi(H)] + J_{12}\langle S\rangle^2$, where the last part is obtained by a Taylor expansion around ϕ_0. $\Delta\phi(H)$ is the field-induced rotation of the moments on sites 3 and 4 in the ac plane. The PO_4 tetrahedra displacement x introduces an asymmetry in the exchange paths increasing $J_{34} \to J + \lambda x$ and decreasing $J_{12} \to J - \lambda x$ (λ is a proportionality constant). This leads to a reduction of the SE energy $\Delta\mathcal{E} =$

$\langle S\rangle^2[-1.26\lambda x - 0.97\lambda x\Delta\phi(H)]$. The displacement of the PO_4 tetrahedra in the lattice is associated with an elastic energy $\epsilon_x x^2$. Minimizing the sum of the SE and elastic energy yields the equilibrium tetrahedral displacement x, proportional to the bulk polarization via $P_x = \mathcal{K}x$:

$$P_x = \frac{\mathcal{K}\langle S\rangle^2\lambda}{\epsilon_x}[0.63 + 0.48\Delta\phi(H)],$$

where $\mathcal{K}$ connects the microscopic charge displacement of the PO_4 tetrahedra to bulk electric polarization. Since this model applies for both phases I and IV, we proceed to use the measured ME response in phase I to estimate the ratio $\frac{\mathcal{K}\lambda}{\epsilon_x}$, enabling us to predict the ME response in phase IV. In phase I, the polarization is described by $P_x = \frac{\mathcal{K}\lambda}{\epsilon_x}\langle S\rangle^2\phi_c\Delta\phi$ [28]. A quadratic onset of $P_x(H_z)$ is evident in Fig. 1. This is due to a constant angle between moments on sites 1 and 2 when $\Delta\phi \to \phi_c$ where the low-angle quadratic terms of an expansion of the SE energy for the two ion pairs (3,4) and (1,2) no longer cancel out (see Appendix B). The quadratic response was fitted to set in at 6.5 T with increasing field, where the measured polarization is $P_x = \mathcal{K}x = 4.6 \times 10^{-7}\frac{\mu C}{cm^2}$. At $\Delta\phi = \phi_c = 0.27$ rad [28], we estimate $\frac{\mathcal{K}\lambda\langle S\rangle^2}{\epsilon_x} \approx 6.2 \times 10^{-6}\frac{\mu C}{cm^2}$. In phase IV, the magnetization increases from $0.45\mu_B$ to $0.5\mu_B$ representing a change in canting angle of $\Delta\phi = 0.13$ rad for ions 3 and 4. Using the estimate for $\frac{\mathcal{K}\lambda\langle S\rangle^2}{\epsilon_x}$, a linear change in the polarization in the interval $P_x = 3.9$–$4.3 \times 10^{-6}\frac{\mu C}{cm^2}$ going through phase IV is predicted. This corresponds well with the observed polarization in phase IV as evident in Fig. 1, strongly supporting the establishment of a longitudinal C_z structure in phase IV.

C. Magnetic structure in phase V

The data shown in Fig. 1(a) indicate that the magnetization is $m \simeq (1/3)m_S$ and slowly varying with field. The neutron diffraction data in Fig. 2(d) display two Bragg peaks at (0,1,0) and (0,4/3,0). As shown in Appendix A, no additional peaks were observed. It is therefore likely that the structure is a longitudinal spin-flip type structure, mainly composed of a $k = 0$ ferromagnetic F_z component (the magnetization) and a C_z component with a commensurate ordering wave vector $k = 1/3$. Note that a C_z component $(+, +, -\beta, -\beta)$ with $k = 1/3$ is equivalent to an F_z component $(+, +, +\beta, +\beta)$ with $k = 2/3$, both being fully compensated AFM structures. The DM interaction is expected to produce weak components transverse to the c axis, but the resulting low-intensity Bragg peaks reflecting these minor components are not observable. When using the weak $D_x = 0.413$ meV anisotropy in a mean-field calculation similar to that presented in Ref. [30], a $k = 1/3$ C_z magnetic structure with spins almost entirely aligned along the c axis is stabilized. The spin components in the bc plane are shown in Fig. 3(c) (see also Appendix C). Phase V does not display the ME effect and the calculated structure obeys this constraint. However it does not produce the observed (0,1,0) reflection. As mentioned earlier, this peak is probed only near the phase boundary between phases IV and V and could have its origin in phase coexistence. The existence of a (0,1,0) Bragg peak in phase V is therefore subject to further investigation. We emphasize that the zero-field Hamiltonian is unable to predict the magnetic structure in phase IV, and therefore the mean-field predictions for phase V should be treated with caution. Clarifying the magnetic structure in phase V requires additional neutron scattering studies.

V. CONCLUSION

To conclude, we have discovered the reentrance of a magnetoelectric response between 19 T and 21 T in $LiNiPO_4$ for fields applied along the c axis. Pulsed-field neutron Laue diffraction reveals a commensurate magnetic structure in this phase, characterized by the propagation vector (0,1,0). We have shown that a magnetized version of the zero-field structure is consistent with all data. This is confirmed by a quantitative model for $P_x(H_z)$ which is in excellent agreement with the data. For fields in the range between 21 T and 30 T we propose a spin-flip type structure with ordering vector (0,1/3,0) and spins nearly parallel to the c axis. In this phase the magnetoelectric effect is absent. A mean-field model employing the zero-field exchange couplings and single-ion anisotropies fails to predict the magnetic structure in the high-field magnetoelectric phase. This indicates that the couplings between magnetic and structural degrees of freedom have a strong influence on the physical properties of $LiNiPO_4$.

Note Added. A very recent paper [45] reports an experimental study of the magnetoelectric effect in $LiNiPO_4$ in pulsed fields. The paper confirms the existence of a magnetoelectric phase near 20T as well as a nonlinear contribution to the magnetoelectric effect in phase I.

ACKNOWLEDGMENTS

We thank N. H. Andersen for discussions. This work was supported by the Danish Agency for Science, Technology, and Innovation under DANSCATT. Research at Ames Laboratory was supported by the US Department of Energy, Office of Basic Energy Sciences, Division of Materials Sciences and Engineering, under Contract No. DE-AC02-07CH11358. A portion of this research used resources at the Spallation Neutron Source, a DOE Office of Science User Facility operated by the Oak Ridge National Laboratory. H.N. acknowledges support by KAKENHI 23224009, ICC-IMR, and MD program.

R.T.-P. and E.F. contributed equally to this work.

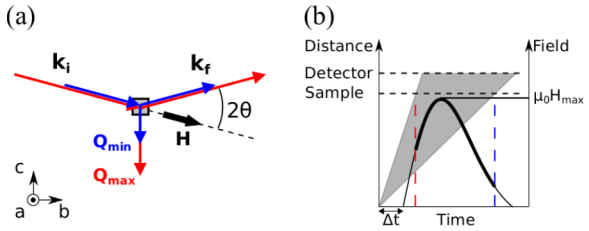

FIG. 4. Experimental setup. (a) Scattering geometry with the magnetic field direction and crystallographic directions indicated. The red (blue) arrows represent the shortest (longest) accessible wavelengths. (b) Neutron travel distance and magnetic field strength as a function of time. The overlap of the neutron pulse (gray area) and magnet pulse (black curve) is determined by the maximum field strength, $\mu_0 H_{max}$, and the time delay, Δt. The red (blue) dashed line corresponds to TOF of the shortest (longest) accessible wavelength.

TABLE I. Magnet settings used in the neutron experiment. The field was generated by a 5.6 mF capacitor bank with a maximum charging level of 1.5 kV corresponding to $\mu_0 H_{\max} = 30$ T.

$\mu_0 H_{\max}$ (T)	19.2	19.2	19.2	19.2	20.7	22.0	22.7	25.2	28.2
Δt (μs)	360	600	750	1200	300	0	700	700	700
No. of pulses	193	73	117	151	119	127	163	202	266

This manuscript has been authored by UT-Battelle, LLC under Contract No. DE-AC05-00OR22725 with the US Department of Energy. The United States Government retains and the publisher, by accepting the article for publication, acknowledges that the United States Government retains a nonexclusive, paid-up, irrevocable, worldwide license to publish or reproduce the published form of this manuscript, or allow others to do so, for United States Government purposes. The Department of Energy will provide public access to these results of federally sponsored research in accordance with the DOE Public Access Plan (http://energy.gov/downloads/doe-public-access-plan).

APPENDIX A: FURTHER EXPERIMENTAL DETAILS

The scattering geometry in the pulsed-field experiment and the principle of controlling the overlap between the magnet and neutron pulses are illustrated in Fig. 4. Table I lists the magnet settings employed as well as the number of magnet pulses discharged for each setting.

In Fig. 5 we show a SEQUOIA detector image in which we have integrated over all field pulses. Only a small detector area around the forward-scattering direction is accessible. This is due to neutron-absorbing boron shielding around the magnet and the sample space. Within the illuminated portion of the detector we only observe Bragg peaks around the expected $(0,K,0)$ position. A careful search for peaks of other forms, e.g., (1,1,0), (1,1.33,0), and (1,2,0), was conducted. No such peaks could be observed in this experiment.

In the interval between the field pulses, the instrument collected zero-field data. Due to the long waiting times, the statistical quality of these data, shown in Fig. 6, is very good.

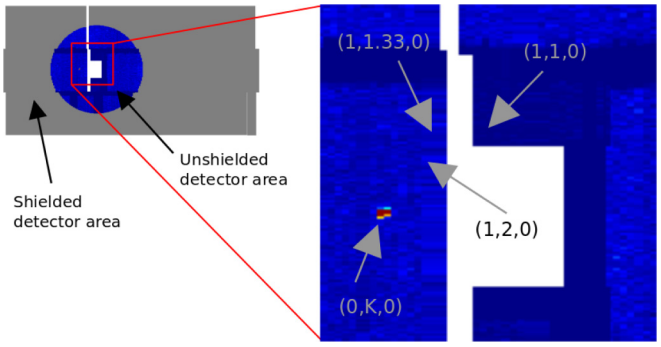

FIG. 5. SEQUOIA detector image integrated over all magnetic field pulses. In the part of the detector not affected by the shielding around the magnet insert, only peaks of the type $(0,K,0)$ were identified.

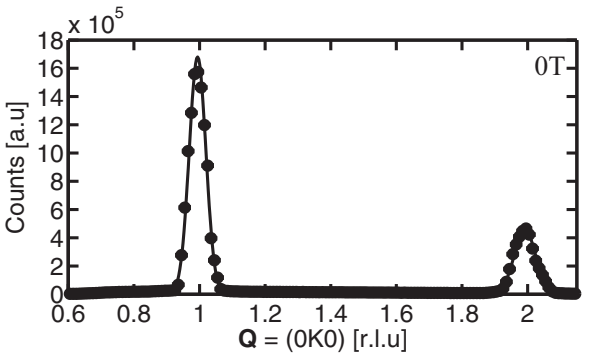

FIG. 6. All neutron counts obtained in zero field as a function of scattering vector $\mathbf{Q} = (0,K,0)$.

As expected, we observe two Bragg peaks in phase I: a nuclear $(0,2,0)$ peak and a magnetic $(0,1,0)$ peak.

The limited statistics of having only counted 1274 neutrons for finite fields exclusively allows for the determination of the Bragg peak positions and not for any quantitative analysis of the intensities. The peak centers are determined by fitting Gaussian line shapes to the data. The peak widths were fixed to values obtained by a linear extrapolation based on the zero-field data shown in Fig. 6.

For each magnet setting, a curve in $(\mu_0 H, K)$ space is probed. The scattered neutrons were recorded in event mode allowing us to assign a corresponding field value (at the sample position) for each individual detected neutron. In Fig. 2 it is evident that some neutron counts occur away from the solid lines representing the corresponding values of $\mathbf{Q} = (0,K,0)$ and magnetic field, $\mu_0 H$. The reason is that the scattered neutrons are spread over two vertical detector tubes, each with signal in 10 pixels. The resulting variation in scattering angle gives rise to a slight difference in flight path. This, in turn, implies that for a given setting of the maximum field strength and delay time, any given value of $\mathbf{Q} = (0,K,0)$ is probed over a small distribution of fields. This is shown in Fig. 7 for the particular case of the data set obtained with $\mu_0 H_{\max} = 28.2$ T and $\Delta t = 700$ μs.

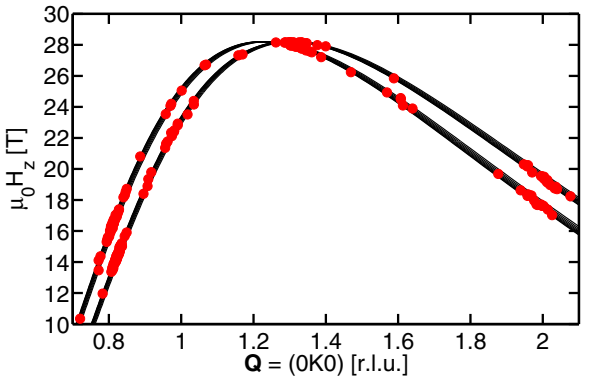

FIG. 7. The effect of having the $(0,K,0)$ Bragg peak signals distributed over multiple pixels in two adjacent detector tubes. The probed curve in $(\mu_0 H, K)$ space is split into two curves which are broadened due to the spread in pixels, as indicated by the curve widths.

TABLE II. The exchange parameters (in units of meV) used in the mean-field model, including the number of neighbors (Z) using the same notation as in Ref. [30].

	J_{bc}^{nn}	J_b'	J_c'	J_{ab}	J_{ac}	J_b^c	J_{bc}^{nnn}
Z	4	2	2	2 + 2	2 + 2	4	4
$J(ij)$	1.002	1.13	0.40	0.321	−0.112	−0.23	−0.08

APPENDIX B: ONSET OF QUADRATIC POLARIZATION IN PHASE I

In phase I, the energy $\mathcal{E}_{12,34}^{\mathrm{SE}}$ of the Hamiltonian $\mathcal{H}_{12,34}^{\mathrm{SE}} = J_{12}\mathbf{S}_1 \cdot \mathbf{S}_2 + J_{34}\mathbf{S}_3 \cdot \mathbf{S}_4$ can be Taylor expanded

$$\mathcal{E}_{\mathrm{SE}} = (J_{12} + J_{34})\langle S\rangle^2\left[1 - \frac{1}{2}(\phi_c^2 + \Delta\phi^2)\right] - (J_{34} - J_{12})\langle S\rangle^2\phi_c\Delta\phi,$$

where $\Delta\phi$ is the field-induced change in canting angle. Assuming that the resulting asymmetry in canting angles changes $J_{12} = J_{34}$ to produce $J_{12} = J - \delta$ and $J_{34} = J + \delta$, only the last term contributes to the resulting change in superexchange energy $\Delta\mathcal{E}_{\mathrm{SE}} = -2\delta\langle S\rangle^2\phi_c\Delta\phi$. This linear dependence on $\Delta\phi$ is shown in Ref. [28] to produce a linear ME response at low fields. However, if the field is strong enough, $\Delta\phi \to \phi_c$, resulting in constant alignment of spins 1 and 2. This activates the first term in the Taylor expansion as a source of ME response. Using the same procedure as in the main text, a Taylor expansion of the superexchange energy around $2\phi_c$ now yields

$$\mathcal{E}_{\mathrm{SE}} = J_{34}\langle S\rangle^2\left[\cos(2\phi_c) - 2\phi_c\Delta\phi - \frac{\cos(2\phi_c)}{2}\Delta\phi^2\right] + J_{12}\langle S\rangle^2$$

using the small-angle approximation for $\sin(2\phi_c)$. Assuming the linear change in exchange constants the energy difference now becomes

$$\Delta\mathcal{E}_{\mathrm{SE}} = \langle S\rangle^2\left(-0.15 - 2\delta\phi_c\Delta\phi - \frac{\delta\cos(2\phi_c)}{2}\Delta\phi^2\right). \tag{B1}$$

Using the same assumptions as in the main text, this gives rise to a continuation of the lower-field ME response through the linear term, with an additional quadratic component as $\Delta\phi > \phi_c$, with tetrahedra displacement given by $x = \frac{\langle S\rangle^2\lambda}{2\epsilon_x}(0.15 + \phi_c\Delta\phi + \frac{\cos(2\phi_c)}{2}\Delta\phi^2)$. Assuming $\Delta\phi \propto M = \chi_c H_z$, we can fit P_x vs H_z in phase I to the function $P_x = c_1 H_z + c_2 S_{c_3}(H_z)(H_z - c_3)^2$, where the c_i are variables and $S_{c_3}(H_z)$ is a Heaviside step function centered at $H_z = c_3$. The step function roughly represents the crossover regime between the two cases described. The quadratic onset thus has a clear justification using the employed model, and can be said to arise from $\Delta\phi \to \phi_c$.

TABLE III. The stabilized $\mathbf{Q} = (0,1/3,0)$ structure at $\mu_0 H \geqslant 23$ T. Due to the spin anisotropy $S_y = 0$ for all ions.

Unit cell 1	ion 1	ion 2	ion 3	ion 4
S_x	0.042	−0.042	0.042	−0.042
S_z	0.985	0.985	0.985	0.985
Unit cell 2	ion 5	ion 6	ion 7	ion 8
S_x	0.236	−0.236	0.042	−0.042
S_z	−0.962	−0.962	0.985	0.985
Unit cell 3	ion 9	ion 10	ion 11	ion 12
S_x	0.042	−0.042	0.236	−0.236
S_z	0.985	0.985	−0.962	−0.962

APPENDIX C: ELABORATION ON THE MEAN-FIELD MODEL

The mean-field model employed in this work was originally introduced in Ref. [30]. The Hamiltonian is assumed to be

$$\mathcal{H} = \frac{1}{2}\sum_{ij} J(ij)\mathbf{S}_i \cdot \mathbf{S}_j + \mathcal{H}_{\mathrm{DM}} + \sum_{\alpha,i} D_\alpha S_{\alpha i}^2 - g\mu_B\sum_i \mathbf{H}\cdot\mathbf{S}_i$$

with $g = 2.2$. Assuming only nearest neighbors to contribute, the DM interaction allowed by symmetry is [28]

$$\mathcal{H}_{\mathrm{DM}} = D_{14}\sum_{ij\in\mathrm{n.n.}}[S_z(1i)S_x(4j) - S_x(1i)S_z(4j) + S_z(3i)S_x(2j) - S_x(3i)S_z(2j)],$$

where, e.g., $S_z(1i)$ only contributes to the sum if the ith site belongs to sublattice 1 consisting of ions on position $\mathbf{r}_1$. The exchange constants used in the Hamiltonian are given in Table II. In order to stabilize structures with short modulation wavelengths, a weak next-nearest neighbor interaction along the b axis between sublattices 1 and 4 in the bc plane, J_{bc}^{nnn}, is introduced. For calculating the structure in phase V, the modulation period along the b axis was fixed to 3 unit cells ($K = 1/3$), which was also found to be the most stable modulation above approximately 23 T in the model with $J_{bc}^{nnn} = -0.08$ meV. The resulting components (thermal mean values) of S_x and S_z on each of the 12 sites are given in Table III. The S_y components of the spins have been omitted as they are all zero, due to the strong D_y term.

[1] W. Eerenstein, N. D. Mathur, and J. F. Scott, Nature (London) **442**, 759 (2006).
[2] H. Schmidt, Ferroelectrics **162**, 317 (1994).
[3] G. A. Smolenskii and I. E. Chapuis, Sov. Phys. Usp. **25**, 475 (1983).
[4] C. Israel, N. D. Mathur, and J. F. Scott, Nat. Mater. **7**, 93 (2008).
[5] Y. Geng, Hena Das, Aleksander L. Wysocki, Xueyun Wang, S.-W. Cheong, M. Mostovoy, Craig J. Fennie, and Weida Wu, Nat. Phys. **13**, 163 (2014).
[6] M. Bibe and A. Barthelemy, Nat. Mater. **7**, 425 (2008).

[7] Claude Chappert, Albert Fert, and Frederic Nguyen Van Dau, Nat. Mater. **6**, 813 (2007).

[8] N. Hur, S. Park, P. A. Sharma, J. S. Ahn, S. Guha, and S-W. Cheong, Nature (London) **429**, 392 (2004).

[9] J. T. Heron, J. L. Bosse, Q. He, Y. Gao, M. Trassin, L. Ye, J. D. Clarkson, C. Wang, Jian Liu, S. Salahuddin, D. C. Ralph, D. G. Schlom, J. Iniguez, B. D. Huey, and R. Ramesh, Nature (London) **516**, 370 (2014).

[10] V. V. Kruglyak, S. O. Demokritov, and D. Grundler, J. Phys. D **43**, 264001 (2010).

[11] Wei Chen and Manfred Sigrist, Phys. Rev. Lett. **114**, 157203 (2015).

[12] A. Pimenov, A. A. Mukhin, V. Yu. Ivanov, V. D. Travkin, A. M. Balbashov, and A. Loid, Nat. Phys. **2**, 97 (2006).

[13] S. W. Cheong and M. Mostovoy, Nat. Mater. **6**, 13 (2007).

[14] A. Scaramucci, E. Bousquet, M. Fechner, M. Mostovoy, and N. A. Spaldin, Phys. Rev. Lett. **109**, 197203 (2012).

[15] T. Kimura, T. Goto, H. Shintani, K. Ishizaka, T. Arima, and Y. Tokura, Nature (London) **426**, 55 (2003).

[16] Masakazu Matsubara, Sebastian Manz, Masahito Mochizuki, Teresa Kubacka, Ayato Iyama, Nadir Aliouane, Tsuyoshi Kimura, Steven L. Johnson, Dennis Meier, and Manfred Fiebig, Science **348**, 1112 (2015).

[17] M. Kenzelmann, A. B. Harris, S. Jonas, C. Broholm, J. Schefer, S. B. Kim, C. L. Zhang, S.-W. Cheong, O. P. Vajk, and J. W. Lynn, Phys. Rev. Lett. **95**, 087206 (2005).

[18] K. Taniguchi, N. Abe, T. Takenobu, Y. Iwasa, and T. Arima, Phys. Rev. Lett. **97**, 097203 (2006).

[19] M. Baum, J. Leist, Th. Finger, K. Schmalzl, A. Hiess, L. P. Regnault, P. Becker, L. Bohaty, G. Eckold, and M. Braden, Phys. Rev. B **89**, 144406 (2014).

[20] Andrei Malashevich, Sinisa Coh, Ivo Souza, and David Vanderbilt, Phys. Rev. B **86**, 094430 (2012).

[21] Maxim Mostovoy, Andrea Scaramucci, Nicola A. Spaldin, and Kris T. Delaney, Phys. Rev. Lett. **105**, 087202 (2010).

[22] M. Mercier, Ph.D. thesis, Université de Grenoble, 1969.

[23] I. Kornev, M. Bichurin, J.-P. Rivera, S. Gentil, H. Schmid, A. G. M. Jansen, and P. Wyder, Phys. Rev. B **62**, 12247 (2000).

[24] V. I. Fomin, V. P. Gnezdilov, V. S. Kurnosov, A. V. Peschanskii, A. V. Yeremenko, H. Schmid, J.-P. Rivera, and S. Gentil, Low Temp. Phys. **28**, 203 (2002).

[25] Yu. N. Kharchenko, N. F. Kharcheno, M. Baran, and R. Szymczak, Low Temp. Phys. **29**, 579 (2003).

[26] T. B. S. Jensen, N. B. Christensen, M. Kenzelmann, H. M. Rønnow, C. Niedermayer, N. H. Andersen, K. Lefmann, M. Jiménez-Ruiz, F. Demmel, J. Li, J. L. Zarestky, and D. Vaknin, Phys. Rev. B **79**, 092413 (2009).

[27] K. Yamauchi and S. Picozzi, Phys. Rev. B **81**, 024110 (2010).

[28] Thomas Bagger Stibius Jensen, Niels Bech Christensen, Michel Kenzelmann, Henrik Moodysson Rønnow, Christof Niedermayer, Niels Hessel Andersen, Kim Lefmann, Jürg Schefer, Martin v. Zimmermann, Jiying Li, Jerel L. Zarestky, and David Vaknin, Phys. Rev. B **79**, 092412 (2009).

[29] D. Vaknin, J. L. Zarestky, J.-P. Rivera, and H. Schmid, Phys. Rev. Lett. **92**, 207201 (2004).

[30] Rasmus Toft-Petersen, Jens Jensen, Thomas Bagger Stibius Jensen, Niels Hessel Andersen, Niels Bech Christensen, Christof Niedermayer, Michel Kenzelmann, Markos Skoulatos, Manh Duc Le, Kim Lefmann, Sonja Rosenlund Hansen, Jiying Li, Jerel L. Zarestky, and David Vaknin, Phys. Rev. B **84**, 054408 (2011).

[31] V. M. Khrustalyov, V. N. Savitsky, and N. F. Kharchenko, Czech. J. Phys. **54**, 27 (2004).

[32] H. Nojiri, S. Yoshii, M. Yasui, K. Okada, M. Matsuda, J.-S. Jung, T. Kimura, L. Santodonato, G. E. Granroth, K. A. Ross, J. P. Carlo, and B. D. Gaulin, Phys. Rev. Lett. **106**, 237202 (2011).

[33] S. Yoshii, K. Ohoyama, K. Kurosawa, H. Nojiri, M. Matsuda, P. Frings, F. Duc, B. Vignolle, G. L. J. A. Rikken, L.-P. Regnault, S. Michimura, and F. Iga, Phys. Rev. Lett. **103**, 077203 (2009).

[34] J. P. C. Ruff, Z. Islam, J. P. Clancy, K. A. Ross, H. Nojiri, Y. H. Matsuda, H. A. Dabkowska, A. D. Dabkowski, and B. D. Gaulin, Phys. Rev. Lett. **105**, 077203 (2010).

[35] S. Gerber, H. Jang, H. Nojiri, S. Matsuzawa, H. Yasumura, D. A. Bonn, R. Liang, W. N. Hardy, Z. Islam, A. Mehta, S. Song, M. Sikorski, D. Stefanescu, Y. Feng, S. A. Kivelson, T. P. Devereaux, Z.-X. Shen, C.-C. Kao, W.-S. Lee, D. Zhu, and J.-S. Lee, Science **350**, 949 (2015).

[36] G. E. Granroth, A. I. Kolesnikov, T. E. Sherline, J. P. Clancy, K. A. Ross, J. P. C. Ruff, B. D. Gaulin, and S. E. Nagler, J. Phys.: Conf. Ser. **251**, 012058 (2010).

[37] Rasmus Toft-Petersen, Manfred Reehuis, Thomas B. S. Jensen, Niels H. Andersen, Jiying Li, Manh Duc Le, Mark Laver, Christof Niedermayer, Bastian Klemke, Kim Lefmann, and David Vaknin, Phys. Rev. B **92**, 024404 (2015).

[38] M. Akaki, H. Iwamoto, T. Kihara, M. Tokunaga, and H. Kuwahara, Phys. Rev. B **86**, 060413(R) (2012).

[39] Hiroyuki Mitamura, Setsuo Mitsuda, Shunsuke Kanetsuki, Hiroko Aruga Katori, Toshiro Sakakibara, and Koichi Kindo, J. Phys. Soc. Jpn. **76**, 094709 (2007).

[40] T. Kimura, Annu. Rev. Mater. Res. **37**, 387 (2007).

[41] J. P. Rivera, Eur. Phys. J. B **71**, 299 (2009).

[42] L. Neel, Ann. Phys. (Paris) **18**, 5 (1932).

[43] M. Fischer and D. R. Nelson, Phys. Rev. Lett. **32**, 1350 (1974).

[44] I. Abrahams and K. S. Easson, Acta Crystallogr., Sect. C: Cryst. Struct. Commun. **49**, 925 (1993).

[45] V. M. Khrustalyov, V. M. Savytsky and M. F. Kharchenko, Low Temp. Phys. **42**, 1126 (2016).